applied sciences

MDPI

Article

Hardware Design and Implementation of a High-Precision Optically Pumped Cesium Magnetometer System Based on the Human-Occupied Vehicle Platform

Keyu Zhou [1], Qimao Zhang [1,2] and Qisheng Zhang [1,*]

[1] School of Geophysics and Information Technology, China University of Geosciences (Beijing), Beijing 100083, China; keyuzhou@email.cugb.edu.cn (K.Z.); zhangqm@aircas.ac.cn (Q.Z.)
[2] Aerospace Information Research Institute, Chinese Academy of Sciences, Beijing 100094, China
* Correspondence: zqs@cugb.edu.cn

Abstract: High-precision magnetometers play a crucial role in ocean exploration, geophysical prospecting, and military and security applications. Installing them on human-occupied vehicle (HOV) platforms can greatly enhance ocean exploration capabilities and efficiency. However, most existing magnetometers suffer from low sensitivity and excessively large size. This study presents a high-sensitivity, miniaturized magnetometer based on cesium optically pumped probes. The designed magnetometer utilizes a three-probe design to eliminate the detection dead zone of the cesium optically pumped probe and enable three-dimensional magnetic detection. The proposed magnetometer uses a flux gate probe to detect the three-axis magnetic field and ensure that the probe does not enter the dead zone. The three probes can automatically switch by measuring the geomagnetic elements and real-time attitude of the HOV platform. This article primarily introduces the cesium three-probe optically pump, flux gate sensor, and automatic switching scheme design of the above-mentioned magnetometer. Moreover, it is proven through testing that the core indicators, such as the accuracy and sensitivity of the cesium three-probe optically pumped and flux gate sensor, reach international standards. Finally, the effectiveness of the automatic switching scheme proposed in this study is demonstrated through drone-mounted experiments.

Keywords: magnetometer; cesium optically pumped probe; flux gate probe; human-occupied vehicle

Citation: Zhou, K.; Zhang, Q.; Zhang, Q. Hardware Design and Implementation of a High-Precision Optically Pumped Cesium Magnetometer System Based on the Human-Occupied Vehicle Platform. *Appl. Sci.* **2024**, *14*, 6778. https://doi.org/10.3390/app14156778

Academic Editor: Roberto Zivieri

Received: 3 July 2024
Revised: 31 July 2024
Accepted: 31 July 2024
Published: 2 August 2024

1. Introduction

High-precision magnetometers play a crucial role in ocean exploration, geophysical prospecting, security and military operations, environmental monitoring, diagnostics, and medicine owing to their exceptional measurement capabilities. These magnetometers can accurately detect the distribution of minerals deep beneath the seabed [1,2] and provide key geological information for the extraction of various resources [3–5], including oil, natural gas, and rare earth elements. Moreover, they are used to monitor the integrity of subsea pipelines and cables to ensure safe and efficient communication and energy transmission [6]. In medicine, they can be used for the calibration and monitoring of magnetic resonance imaging (MRI), diagnosis of magnetoencephalography (MEG), and magnetocardiography (MCG) [7]. In scientific research, magnetometers are employed to measure minute changes in the Earth's magnetic field, which is essential for understanding geomagnetic variations [8–11], identifying crustal movements [12], and monitoring seismic activities and other natural phenomena. In marine archaeology, optically pumped cesium magnetometers are used to help locate ancient shipwrecks and other cultural heritage sites and provide unique insights into historical research and cultural preservation [13]. In military and security fields, these devices are utilized to monitor and defend underwater borders and identify and track potential threats, such as submarines or mines, thereby enhancing security.

Specifically, when optically pumped cesium magnetometers are installed on platforms such as human-occupied vehicles (HOVs) [14], researchers can directly carry high-precision instruments to the seafloor to conduct detailed geological surveys and on-site data collection. The application of HOV platforms enables magnetometers to operate in extreme deep-sea environments and allows researchers to make decisions based on real-time data monitoring and analysis. This has revolutionary significance for deep-sea scientific research, resource exploration, and environmental monitoring. Additionally, an optically pumped cesium magnetometer mounted on an HOV provides valuable data for marine biodiversity studies, the health monitoring of seabed ecosystems, and long-term impact studies of global climate change [6].

J. Ge et al. studied a towed Overhauser ocean magnetometer for detecting weak magnetic anomalies in 2020. They used an improved adaptive Kalman algorithm to achieve adaptive suppression of magnetic noise in the magnetometer, achieving a sensitivity of 12 pT $Hz^{-1/2}$ @ 1 Hz and a dynamic range of 20,000 nT to 100,000 nT [15]. In 2022, Yu Caoyang et al. analyzed and optimized an autonomous underwater vehicle (AUV) equipped with two three-axis magnetometers for inspecting submarine cables. They proposed a novel two-layer framework that integrates anti-noise cable positioning and robust tracking algorithms to guide AUVs in tracking submarine cables in the presence of sensor noise and ocean currents [16]. Additionally, in 2022, Kai Jin et al. designed a portable VCSEL Pumped Cesium Atomic Magnetometer and compared it with the CS-3. They found that the performance was largely in the same order of magnitude, while their design offered reduced power consumption and a smaller size [17].

With technological advances, it is foreseeable that these magnetometers will have a profound impacts in more fields, promoting the further development of marine science and related technologies. Therefore, it is of great significance to continuously improve and optimize magnetometer systems. In this study, we adopted a combination of an optically pumped cesium magnetometer and a fluxgate probe. The fluxgate probe is used for the magnetic compensation and selective switching of the cesium optically pumped probes to avoid dead zones, thereby improving the sensitivity, gradient tolerance, and dynamic range of the magnetometer. The performance of the optically pumped cesium magnetometer designed in this work was compared with those of the CS-3 and G-824A magnetometers. Our magnetometer was found to be comparable in terms of performance, while exhibiting lower sensitivity (0.29 pT @ 1 sample/s), larger gradient tolerance ($\geq$54,000 nT/m), larger dynamic range (12,165.10–137,992.85 nT), and lighter weight (1.49 kg).

2. Overall Design

The submersible optically pumped cesium magnetometer contains an optically pumped probe, a flux gate probe, a magnetic signal processor, and a high-depth pressure hull. The front ends of the magnetic compensation probe and optically pumped probe are installed in the high-depth pressure hull without any magnetic probes, and the probe electronics unit and magnetic signal processor are installed inside the high-depth electronics pressure hull. The system block diagram is shown in Figure 1.

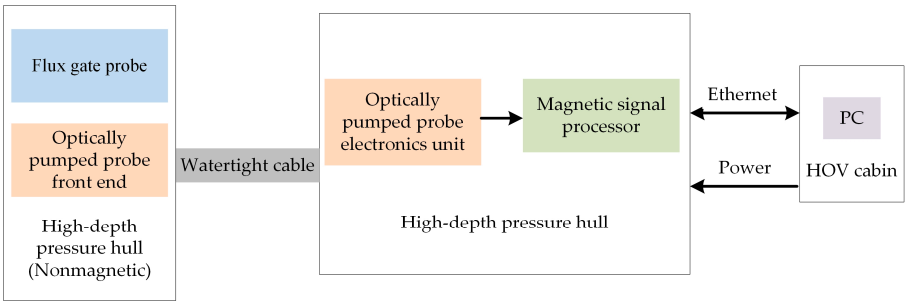

Figure 1. System block diagram.

The optically pumped probe is employed for high-precision scalar magnetic field measurements, achieving accuracy at the pT level. The fluxgate probe assists in selecting the optically pumped probe to circumvent dead zones and mitigate magnetic interference signals arising from the motion and attitude of the submersible platform. Additionally, a magnetic signal processor is utilized for signal processing and data communication with the upper computer.

3. Optically Pumped Probe Design

Each optically pumped probe contains a probe front end and probe electronics unit. The front end primarily senses the total strength of the target magnetic field. The electronics unit drives the probe and outputs the magnetic field frequency signal to the magnetic signal processor. The hardware of the optically pumped probe is shown in Figure 2.

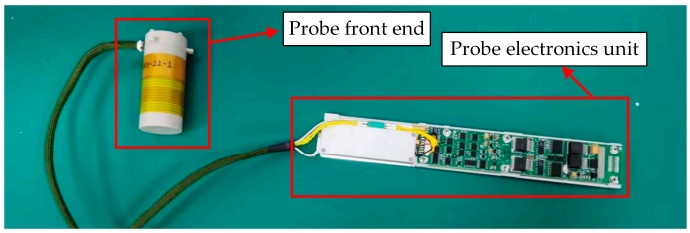

Figure 2. The hardware of the optically pumped probe.

3.1. Probe Front End

The cesium optically pumped probe is a high-sensitivity magnetometer that utilizes the properties of cesium atoms to measure the magnetic field strength [18]. Our design adopts a self-oscillating cesium optically pumped probe structure. The probe model is shown in Figure 3, and the core components include a cesium atomic lamp, optical components, cesium absorption chamber, and high-precision photodetector module. This probe uses a cesium atomic lamp as the core light source to polarize cesium atoms.

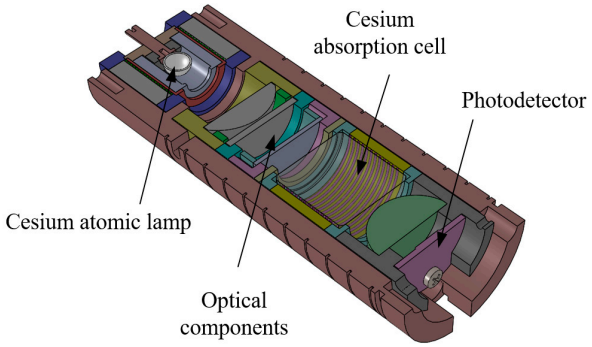

Figure 3. The cesium optically pumped probe.

3.1.1. Cesium Atomic Lamp Design

The cesium atomic lamp comprises a cesium bulb, excitation structure, and non-magnetic heating wire. The design aims to improve the discharge uniformity and sensitivity of the cesium lamp while reducing the thermal consumption of radiofrequency (RF) excitation [19]. The structural model of the cesium atomic lamp is shown in Figure 4, and the physical object is shown in Figure 5. The cesium bulb is spherical and has a diameter of 8 mm, and it contains 800 μg of cesium, filled with 5 Torr of xenon gas as a buffer gas. The sealing tail end is used to fix the cesium bulb and collect excess cesium metal as the cold end. The excitation structure includes an excitation coil, a parallel capacitor, and a shielding copper shell. Combined with the cesium bulb, the structure forms a load that matches the impedance of the RF excitation source, with a resonant frequency of

approximately 165 MHz and a standing wave ratio of less than 1.5, thereby minimizing the thermal consumption of RF excitation. The shielding copper shell is wound with non-magnetic heating wires, using twisted pairs to cancel the additional magnetic field generated by the heating current. A resistance of 45 Ω is used to heat the cesium lamp in low-temperature environments, increasing the initial concentration of cesium atoms in the bulb and achieving rapid ignition under low-temperature conditions.

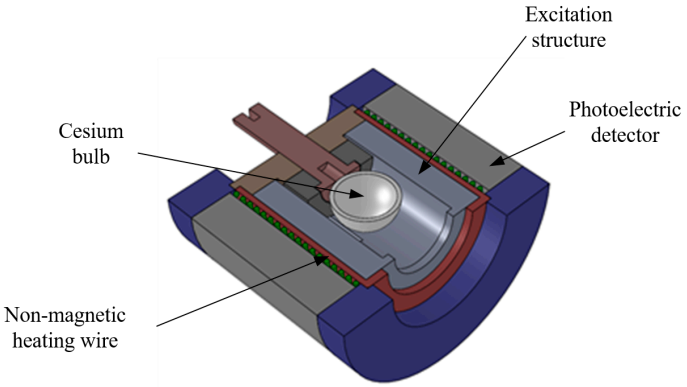

Figure 4. A three-dimensional model of the cesium atomic lamp.

Figure 5. A physical picture of the cesium atomic lamp.

Additionally, the cesium absorption chamber is another key component that is responsible for providing the working substance, ensuring effective interaction between the pump light and cesium atoms. The optical components, including lenses, filters, and polarizers, are designed to optimize the optical path and improve the accuracy of the optically pumped probe. The photoelectric detector is responsible for receiving the optical signal and transmitting it to the signal processing unit, employing a non-magnetic design to avoid magnetic interference. The overall design considers the heating efficiency of the cesium bulb, temperature gradient, and minimization of magnetic field interference to enhance the performance of the probe.

The cesium absorption cell significantly impacts the overall volume of the probe owing to its relatively large size. Therefore, to achieve the goal of miniaturizing the cesium optically pumped probe, it is essential to develop technology for manufacturing smaller atomic absorption cells. When the size of the absorption cell cavity is significantly reduced, the actual filling pressure of the absorption cell is highly susceptible to the sealing temperature of the cavity, causing substantial pressure changes. For each specification of the atomic absorption cell, we precisely measured key parameters, such as the intrinsic linewidth and absorption line frequency shift, maintaining the pressure control accuracy of the absorption cells within 10% across different specifications. The model of the cesium absorption cell is shown in Figure 6. The cesium bulb has a cylindrical design, containing a small amount of high-purity cesium element, with 60 Torr of helium used as the buffer gas. Non-magnetic heating wires are wound around the outer wall of the cesium bulb, with a resistance of 46 Ω, designed as twisted pairs to cancel the additional magnetic field generated by the heating current, thus avoiding interference with magnetic measurements. The outermost layer of the cesium absorption cell contains a non-magnetic thermal insulation material,

designed using high-temperature resistant insulation cotton, which improves the temperature uniformity inside the cesium bulb, thereby minimizing the resonance signal linewidth of the cesium absorption cell.

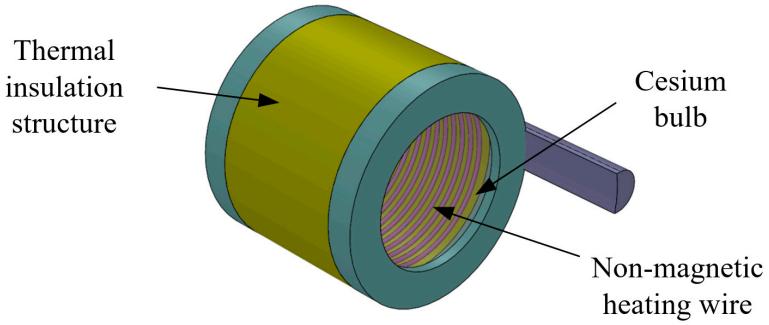

Figure 6. A cesium absorption cell model.

3.1.2. Cesium Absorption Cell Design

The relatively large size of the cesium absorption cell significantly impacts the overall volume of the probe. Therefore, to miniaturize the cesium optically pumped probe, it is essential to develop technology for manufacturing smaller atomic absorption cells. When the size of the absorption cell cavity is significantly reduced, the actual filling pressure of the absorption cell becomes highly susceptible to the sealing temperature of the cavity, resulting in substantial pressure changes. For each specification of the atomic absorption cell, we precisely measured key parameters, such as intrinsic linewidth and absorption line frequency shift, maintaining the pressure control accuracy of the absorption cells within 10% across different specifications. The model of the cesium absorption cell is shown in Figure 6. The cesium bulb has a cylindrical design, containing a small amount of high-purity cesium element, with 7999.34 Pa of helium used as the buffer gas. Non-magnetic heating wires are wound around the outer wall of the cesium bulb, with a resistance of 46 Ω, designed as twisted pairs to cancel the additional magnetic field generated by the heating current, thus avoiding interference with magnetic measurements. The outermost layer of the cesium absorption cell is composed of non-magnetic thermal insulation material, designed with high-temperature-resistant insulation cotton, which improves the temperature uniformity inside the cesium bulb, thereby minimizing the resonance signal linewidth of the cesium absorption cell.

3.2. Electronics Unit Design

The probe electronics unit connects the front end of the probe to the magnetic signal processor. It provides temperature control for the probe's front end and generates excitation signals, processes the signals output by the front end, and outputs magnetic field signals to the magnetic signal processor.

3.2.1. Signal Conditioning Circuit

The signal conditioning circuit filters, amplifies, and conditions the voltage signal output by the photodetector. As shown in Figure 7, the circuit can be divided into five main functional modules: the pre-amplifier circuit, automatic gain control circuit, intermediate amplification stage, phase-shift circuit, and waveform shaping circuit.

The Larmor signal output by the photodetector of the cesium optically pumped probe is first processed by a pre-amplifier, then stabilized by automatic gain control, followed by intermediate amplification. The signal is then sent to the internal feedback coil of the probe through a phase-shift circuit, achieving self-oscillation through positive feedback. Simultaneously, the intermediate output signal is shaped into a square wave by a comparator and output to the frequency measurement circuit, yielding the corresponding external magnetic field strength. Given that the geomagnetic field ranges from 20,000 to 70,000 nT,

in this study, the bandwidth of the signal conditioning circuit was set to 70–245 kHz. The signal conditioning circuit sequentially performs pre-amplification, automatic gain control, intermediate amplification, phase shifting, and comparison within this frequency range.

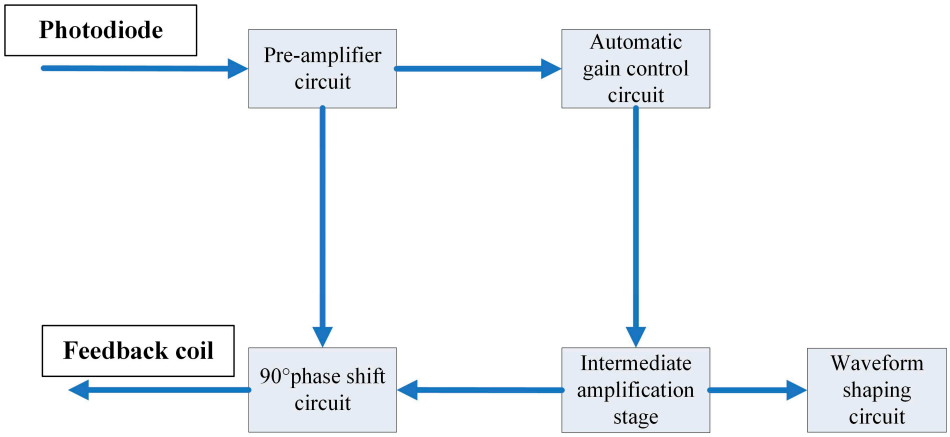

Figure 7. A schematic diagram of the signal conditioning process.

The pre-amplifier circuit converts the photodiode current output by the probe into a voltage signal, constituting a transconductance circuit based on an ultra-low noise amplifier. The signal conditioning circuit diagram is shown in Figure 8. The voltage signal from the pre-amplifier circuit is processed by a controllable gain amplification circuit and an intermediate amplification circuit to output a stable-amplitude sinusoidal signal, the frequency of which is the Larmor frequency. Automatic gain control of the circuit is achieved by performing peak detection on the output signal and feeding it back to the controllable gain amplification circuit. The intermediate amplification circuit adjusts the gain and bandwidth of the circuit. To be more specific, in Figure 8, D3 and D4 (BAS321) are used to protect the circuit from overvoltage. The AD8338 serves as the controllable gain amplifier, with its gain dynamically adjustable by directing the output voltage to the gain control input pin (pin 14).

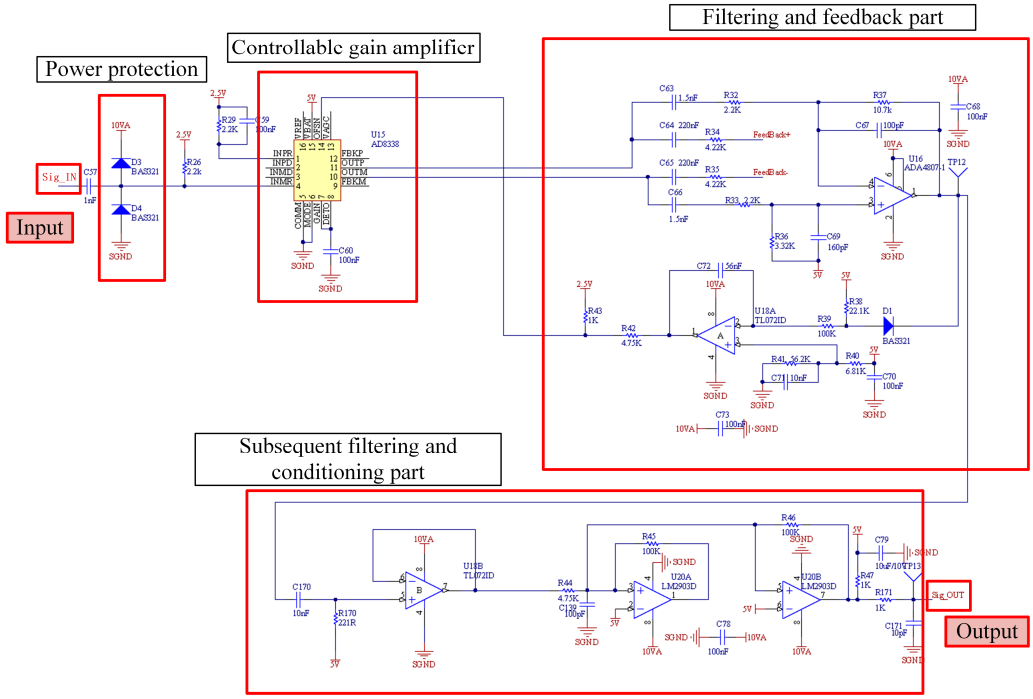

Figure 8. A circuit diagram of the signal conditioning circuit.

3.2.2. Temperature Control Circuit

The cesium lamp and absorption cell in the cesium optically pumped probe require constant temperature control. A schematic diagram of the temperature control circuit is shown in Figure 9. Alternating current (AC) heating was adopted in this study to avoid interference with magnetic field measurements, with a range of −55 °C to 70 °C. The signal generator produces an AC heating signal, which drives the non-magnetic heating wire inside the probe through a power amplifier circuit. The temperature detection circuit monitors the temperature. The constant temperature control circuit implements proportional–integral (PI) control and regulates the output power of the audio amplifier by changing the signal amplitude to control the final temperature. The temperature control circuit design is shown in Figure 10. In this diagram, R1, R2, R3, R4, and the heating coil form a four-arm balanced bridge, while Q1, Q2, Q3, and Q4 form an H-bridge heating circuit that simulates PID control for maintaining a constant temperature. When the bridge is balanced, the heating coil reaches the set temperature, and the H-bridge ceases heating. If the resistance value of the sliding resistor R3 is changed, the temperature can be reset. At this point, the bridge becomes unbalanced, leading to two possible scenarios: First, if the reset temperature is lower than the current temperature, the H-bridge remains inactive, and the system must dissipate heat gradually through the cesium lamp and cesium chamber to reach the new set temperature. Second, if the reset temperature is higher than the current temperature, the H-bridge activates until the set temperature is achieved. This temperature control circuit has two notable characteristics: firstly, it uses an AC signal above 10 kHz for heating, ensuring that the generated AC magnetic field is outside the working bandwidth; secondly, it controls the heating process by monitoring changes in the impedance of the heating coil itself. This means that the heating coil functions both as an actuator in the control system and as a sensor to provide feedback signals to the control system.

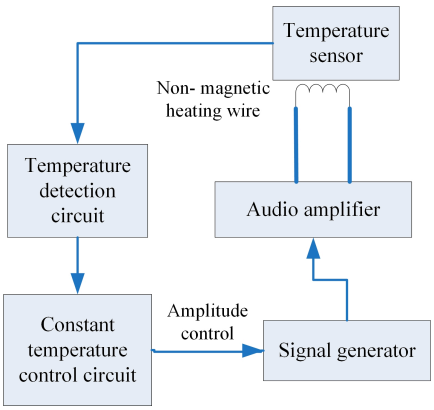

Figure 9. A schematic diagram of the temperature control unit.

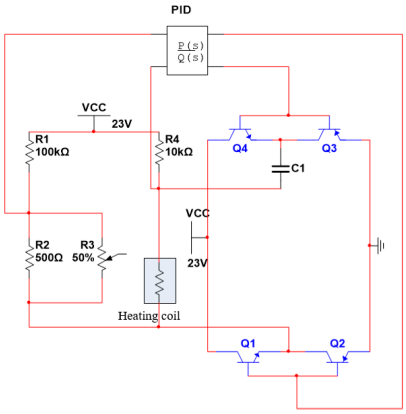

Figure 10. Design diagram of the temperature control circuit.

3.2.3. RF Excitation Circuit

The light source of the optically pumped probe is an electrodeless cesium discharge lamp, which is ignited by a high-frequency excitation source provided by the excitation circuit. This circuit must satisfy the requirements of the excitation frequency and maintain stable output power. A schematic diagram of the circuit is shown in Figure 11. The circuit primarily consists of a voltage-controlled oscillator and an RF power amplifier. The voltage-controlled oscillator can change the operating frequency by controlling the voltage, and the RF power amplifier can adjust the RF output power through gate voltage.

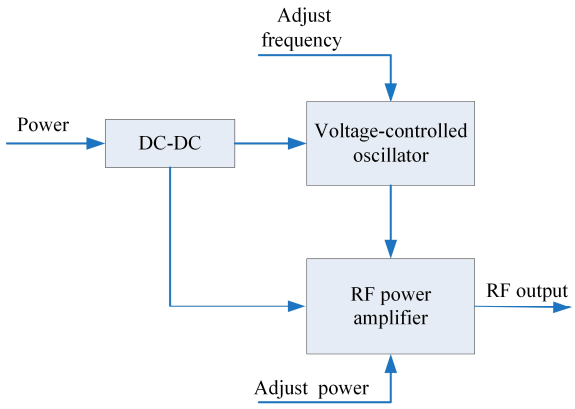

Figure 11. A schematic diagram of the RF excitation circuit.

4. Flux Probe Design

This system utilizes triaxial flux gate technology [20] to capture three-dimensional magnetic vector information of a deep-sea manned submersible within the magnetic field of the Earth. The probe records vector changes in the magnetic field as the submersible undergoes various movements, such as roll, pitch, and yaw. On this basis, it constructs a compensation model to derive compensation parameters, which effectively reduces magnetic interference caused by changes in the submersible attitude and achieves the automatic switching of three cesium optically pumped probes.

4.1. Probe Unit

The probe unit forms the core of the flux gate sensor. The sensing units for the *X*, *Y*, and *Z* axes are precisely arranged on the planes of the probe framework to achieve coaxial alignment and maintain a certain distance, minimizing mutual interference among the three axes. As shown in Figure 12, each single-axis sensing unit comprises a magnetic core, excitation coil, and induction coil, arranged sequentially from inside to outside. Each magnetic core is made from cobalt-based amorphous ribbons composed of CoFeMoSiB. This material has been widely used in magnetic recording and magnetic shielding owing to its high magnetic permeability, low coercivity, and good rectangular hysteresis loop characteristics [21,22]. It is ideal for manufacturing ultra-thin laminated magnetic cores and magnetic switch components and has become a research hotspot in recent years [22,23]. This material is easily magnetized and demagnetized quickly and features narrow hysteresis loops and extremely low hysteresis loss. Therefore, flux gate sensors designed with this magnetic core can realize high sensitivity and low noise. The excitation coils are divided into two groups, wound on two cobalt-based amorphous magnetic cores, and connected end-to-end. Under the resonance effect of the periodic current signal and parallel capacitors, the energy of the excitation signal is efficiently transferred to the magnetic cores. The resulting high-intensity alternating magnetic flux periodically drives the magnetic cores to saturation. The larger induction coils detect the secondary harmonic components generated by the excitation signal, thus obtaining information on the external magnetic field. These coils are placed at the center of the two groups of excitation coils. The placement maximizes

the signal-to-noise ratio (SNR) of the probe and ensures that the induction coils are tightly attached to the magnetic cores.

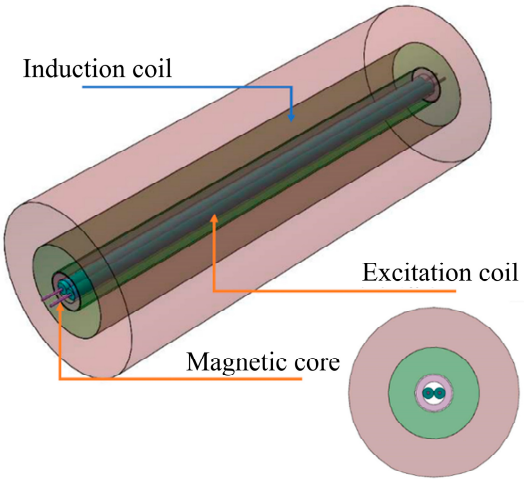

Figure 12. The structure of the single-axis flux gate probe.

Based on this structure, the sensor design parameters are as shown in Table 1.

Table 1. The design parameters of the flux gate probe.

No.	Structure	Design Indicators	
1	Magnetic core	Material Length Diameter	Cobalt-based amorphous ribbons 21 mm ± 0.2 mm 0.2 mm
2	Excitation coil	Wire diameter Number of turns	0.035 mm 500
3	Induction coil	Wire diameter Number of turns	0.2 mm 800

4.2. Electronics Unit

The electronics unit of the flux gate sensor primarily consists of an excitation circuit and a detection circuit.

The excitation circuit comprises a waveform generation circuit, frequency dividers, power amplification circuit, and matching network. Its main function is to provide periodic square wave current signals to ensure that the magnetic core is periodically deeply saturated. The waveform generation circuit uses a crystal oscillator and inverter to produce a 1 MHz oscillation signal, which is then divided by 32 to generate a 31.25 kHz double-frequency signal for the demodulation circuit reference and divided by 64 to generate a 15.625 kHz fundamental frequency signal for the excitation coils. The power amplification circuit further amplifies the power of the fundamental frequency excitation signal to drive the excitation coils, creating a large excitation magnetic field by generating a high current in the excitation coils. The matching circuit uses an impedance network to tune the frequency of the excitation coils and the excitation signal.

The detection circuit demodulates the signal from the induction coils and outputs a voltage signal proportional to the measured strength of the target magnetic field, thus completing the detection of magnetic field signal. Our system employs the commonly used second harmonic detection method. The induced signal and double-frequency signal pass through an analog multiplier to demodulate the signal. The demodulated signal then passes through a low-pass filter circuit, which isolates the useful signal proportional to the strength of the magnetic field. The low-pass filter circuit performs both amplification and filtering. It utilizes a low-noise amplifier (with noise less than 10 nV $Hz^{-1/2}$) and adjusts

the flux gate bandwidth using resistor–capacitor (RC) parameters. The filter bandwidth was set to 1 kHz in this study. The feedback resistor network compensates the flux gate sensor via the feedback coil and adjusts the sensor output response. The circuit diagram is shown in Figure 13.

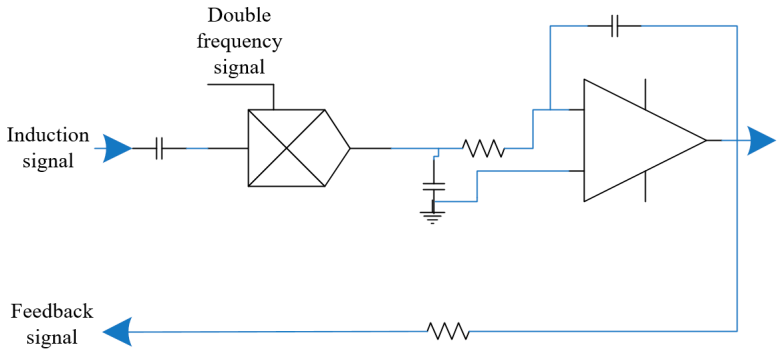

Figure 13. A schematic diagram of the detection circuit.

5. Probe Automatic Switching Scheme

5.1. Three Optically Pumped Probe Structure Design

Regarding the working principle of the cesium optically pumped probe, its measurement range for the incident angle of the external magnetic field is 15° to 75° and 105° to 165°, with dead zones (i.e., loss of lock ranges) in the polar direction from 10° to 15° and 165° to 180° and in the equatorial direction from 80° to 100°. Therefore, a single cesium optically pumped probe, when in operation, risks entering the dead zone as the heading of the submersible or the geomagnetic azimuth of the area to be measured changes. A combination of three optically pumped probes is used to achieve the requirement for the magnetic measurement system to work continuously without loss of lock in any heading and any attitude. By adjusting the installation angle relationships among multiple optically pumped probes, their working angles complement each other. Automatic probe switching and correction algorithms are then used to ensure that the combination of cesium optically pumped probes can operate continuously and normally at any geomagnetic field angle. The three-dimensional dimensions of the optically pumped probe assembly are shown in Figure 14, and the three-dimensional diagram is shown in Figure 15.

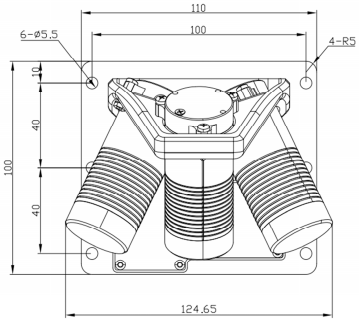

Figure 14. The dimensions of the optical probe unit (unit: mm).

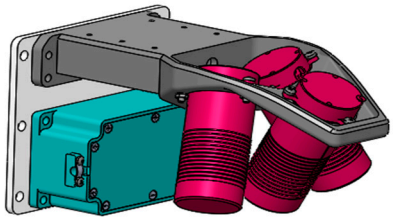

Figure 15. A three-dimensional diagram of the probe assembly.

5.2. Switching Scheme Based on the Minimum Deviation Angle Criterion

Through simulation calculations, using a 45-degree angle between the probe and the geomagnetic field as a reference, the switching scheme based on the minimum deviation angle criterion can determine the probe number that outputs the minimum deviation angle under any heading and geomagnetic inclination conditions. The simulation results are shown in Figure 16.

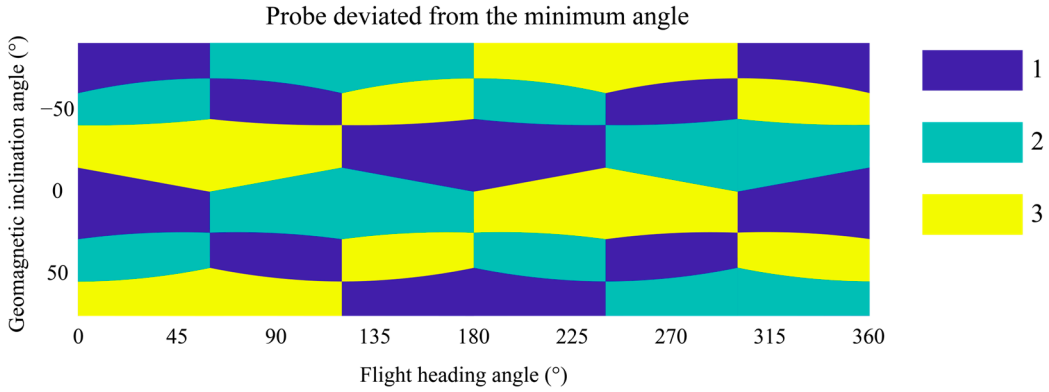

Figure 16. The simulation results.

The switching of the three optically pumped probes is achieved automatically through software, and the switching process is shown in Figure 17. During the switching process, the system calculates geomagnetic elements, attitude, and other related parameters in real time based on fluxgate data and makes switching decisions based on these parameters. Specifically, the system uses the fluxgate to calculate the current magnetic inclination and declination angles, and combined with the known installation angles of the optically pumped probes and the fluxgate, it can determine the angles between the three optically pumped probes and the geomagnetic field. When the angle between the geomagnetic field and the optically pumped probe is 45°, the system will prioritize the optically pumped probe with the optimal working angle. To achieve this, the system subtracts 45° from the angles between each of the three optically pumped probes and the geomagnetic field and then selects the smallest value as the basis for switching.

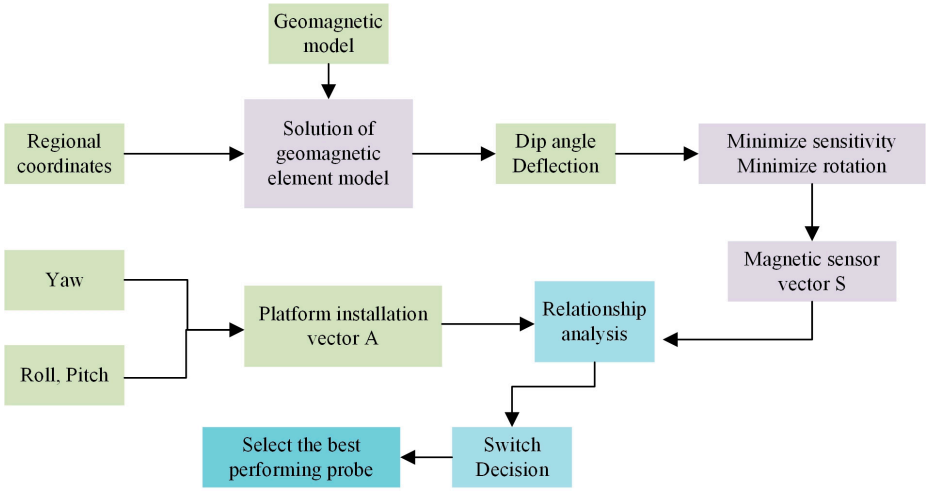

Figure 17. A control flowchart for switching between three probes.

6. Design of Magnetic Signal Processor

The hardware circuit of the magnetic signal processor consists of an acquisition board, power supply board, and digital board. The cesium optically pumped probe detects the total strength of the magnetic field and inputs the Larmor frequency signal into the

acquisition board of the magnetic signal processor. The magnetic compensation probe measures the attitude changes in the HOV platform in the geomagnetic coordinate system and sends the analog signal to the acquisition board of the processor. The magnetic signal processor processes the frequency and analog signals and communicates the data using the HOV platform. The power supply board protects the external power supply. With an input of 10–60 V and an output of 24 V, the power supply board powers the subsequent circuit modules. Additionally, it features overvoltage, overcurrent, and high-temperature protection.

6.1. Acquisition Board Design

The triaxial flux gate typically outputs three-channel analog signals. The principle of the signal acquisition circuit is illustrated in Figure 18. The input signal first passes through an input protection circuit to limit the amplitude and prevent the transient high voltage from damaging subsequent analog channels. The signal then enters the impedance matching network to reduce waveform distortion. Following this, the signal passes through the signal-preprocessing circuit, which provides high-impedance input to the external signal and performs RF filtering of the signal to mitigate aliasing and reduce RF interference. Finally, the signal passes through the analog/digital (A/D) driver and enters the A/D converter (ADC). The field-programmable gate array (FPGA) controls the ADC chip for data acquisition and temporarily stores the collected data in the system memory.

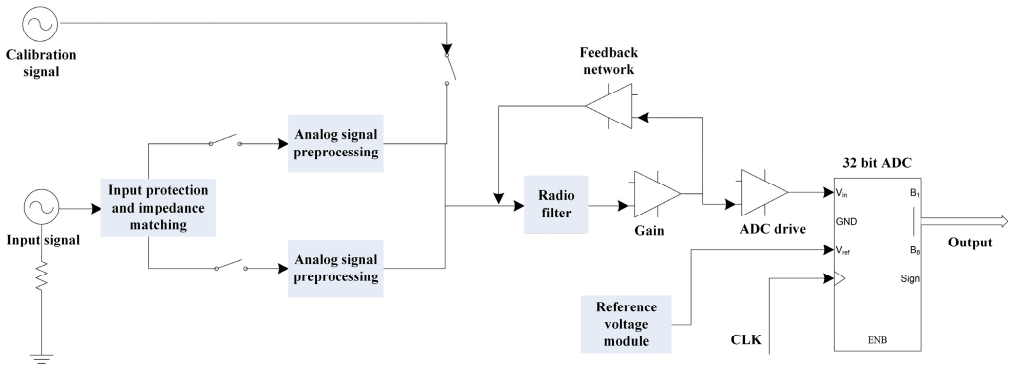

Figure 18. A block diagram of the triaxial flux gate acquisition board.

The digital acquisition section first isolates the Larmor frequency signal from the power line. Subsequently, it performs low-pass filtering on the Larmor signal to eliminate out-of-band noise. Finally, it outputs a low-jitter digital logic signal through a high-speed hysteresis comparator. The high-performance FPGA processes the digital logic signal to calculate and output the magnetic field strength.

6.2. Digital Board Design

The digital processing section utilizes the Zynq XC7Z020 processor chip, manufactured by Xilinx, Inc., headquartered in San Jose, CA, USA [24]. This chip includes an FPGA and a central processing unit (CPU), and it is equipped with 1 GB of memory and 32 GB of storage capacity. The CPU core processing module acts as the control center for the carrier magnetic interference compensation system. It performs system power control and monitoring, self-diagnostics, parameter configuration, raw data acquisition, compensation parameter calculation, real-time compensation computation, and data storage. The peripheral interface of the core board is shown in Figure 19. An industrial-grade TransFlash (TF) card is used to store system files and acquisition data. An Ethernet interface is provided for data communication, and a USB interface is used for system debugging and necessary power modules.

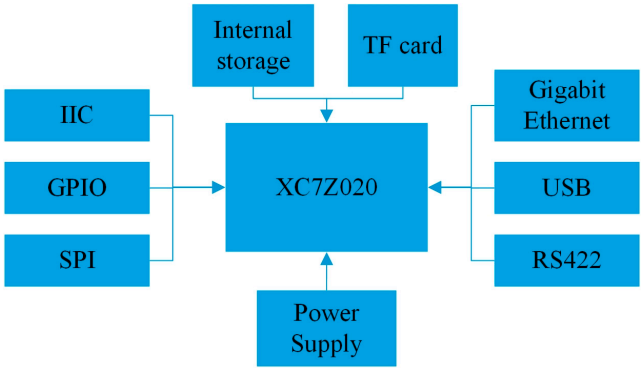

Figure 19. The peripheral circuit of the Zynq XC7Z020 processor chip.

7. Instrument Testing

Rigorous tests were conducted on the core modules of the high-precision optically pumped cesium magnetometer system designed based on the HOV platform, including the optically pumped cesium magnetometer probe and the three-component flux gate probe. The key indicators of the system were compared with those of state-of-the-art products to demonstrate the superior performance achieved.

7.1. Optically Pumped Cesium Magnetometer Probe Testing

The optically pumped cesium magnetometer and its probe were rigorously tested for core indicators, including sensitivity, gradient tolerance, dynamic range, etc. The results are compared with those of leading instruments of the same type, including the CS-3 from Scintrex in Vaughan, ON, Canada [25] and the G-824A from Geometrics in San Jose, CA, USA [26]. The results are presented in Table 2.

Table 2. A comparison of the test results of the optically pumped cesium magnetometer probe with instruments of the same type.

Indicator	Proposed Optically Pumped Cesium Magnetometer	CS-3	G-824A
Absolute accuracy	<2.5 nT	<2.5 nT	<3 nT
Sensitivity	0.29 pT @ 1 sample/s	0.6 pT $Hz^{-1/2}$ rms	0.5 pT $Hz^{-1/2}$ rms
Gradient tolerance	≥54,000 nT/m	40,000 nT/m	19,685 nT/m
Dynamic range	12,165.10–137,992.85 nT	15,000–105,000 nT	20,000–100,000 nT
Direction error	±0.2 nT	±0.2 nT	±0.15 nT
Weight	1.49 kg	1.5 kg	2.7 kg

7.2. Absolute Accuracy Test

To test its absolute accuracy, the optically pumped cesium magnetometer probe was placed inside a torque-free coil located within a magnetic shielding cylinder. The schematic diagram of the test setup is shown in Figure 20. The photo of the magnetic shielding cylinder is shown in Figure 21; the shielding cylinder is equipped with a uniform magnetic field generating coil, which can generate a uniform magnetic field inside the shielding cylinder.

A standard constant magnetic field was generated by the torque-free coil, and the measurement results of the magnetometer were compared with this standard.

$$\overline{B} = \frac{1}{10}\sum_{i=1}^{10} B_i \quad (1)$$

where B_i denotes the total outputted field strength, and n indicates the number of test points. The experimental standard deviation of the observed value, calculated using Equation (2), was taken as the absolute accuracy.

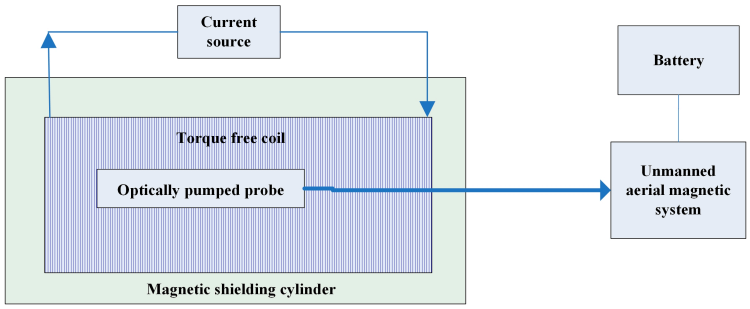

Figure 20. A schematic diagram of the absolute accuracy, sensitivity, and dynamic range testing of the optically pumped cesium magnetometer.

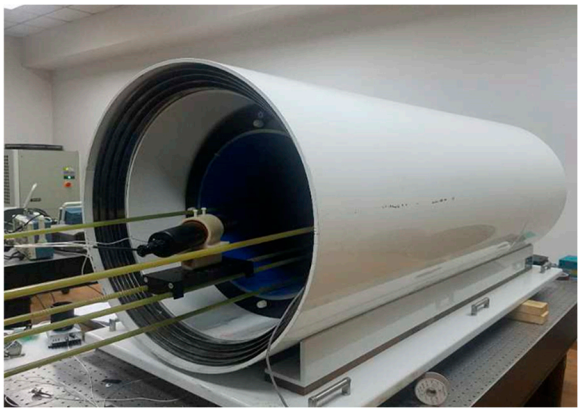

Figure 21. A photograph of the magnetic shielding cylinder.

$$S_B = \pm\sqrt{\frac{\sum_{i=1}^{n}(B_i - \overline{B})^2}{n-1}} \quad (2)$$

The measurement results (Table 2) indicate the absolute accuracy of the proposed optically pumped cesium magnetometer probe, which is less than 2.5 nT, a value that is equivalent to the leading international standard value for such instruments.

7.3. Sensitivity Test

Sensitivity refers to the ability of the optically pumped cesium magnetometer probe to detect the smallest changes in the magnetic field. To test its sensitivity, the proposed optically pumped cesium magnetometer probe was placed in the uniform magnetic field region of a standard magnetic field generation system, with the probe direction forming a 45° angle with the standard magnetic field direction. After the magnetometer stabilized, data were recorded for 2 min. The power spectral density of the magnetic field was analyzed and processed based on the sampling rate S and sample size of the collected data, yielding the power spectral density of the magnetic field. The sensitivity value corresponding to the 1 Hz point in the spectral density data was read, and the results are presented in Table 2.

7.4. Gradient Tolerance Test of the Optically Pumped Cesium Magnetometer Probe

The gradient tolerance of the optically pumped cesium magnetometer probe measures its ability to maintain measurement accuracy and reliability in a non-uniform magnetic field environment. To test this indicator, the target magnetometer probe was placed in a gradient field coil, as shown in Figure 22. The gradient coil was powered to generate a standard gradient magnetic field. By adjusting the current supplied to the gradient coil, the magnetic field strength was increased stepwise. The magnetic field strength detected by the magnetometer was observed. When the magnetometer entered the loss-lock state, the

magnetic field gradient was recorded. This value represents the gradient tolerance of the magnetometer. As indicated in Table 2, the test data suggest that the proposed probe has higher gradient tolerance than leading instruments of the same type. The low direction error shows that it maintained accuracy and stability in magnetic field environments with more rapid changes.

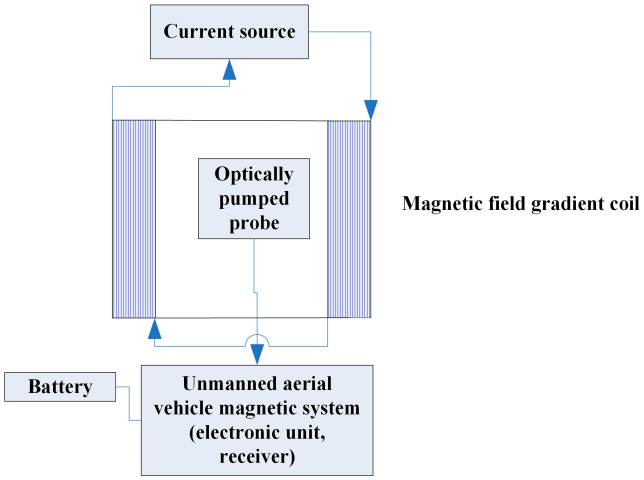

Figure 22. A schematic diagram of gradient tolerance testing for the optically pumped cesium magnetometer.

7.5. Dynamic Range Test of the Optically Pumped Cesium Magnetometer Probe

To test the range of magnetic field strengths that the optically pumped cesium magnetometer probe can measure, i.e., its dynamic range, the probe was placed in a standard magnetic field generation device, as shown in Figure 20. We conducted the test using an ultra-high uniformity magnetic field generation system, as shown in Figure 23. The device generated standard constant magnetic fields B with strengths between 15,000 and 120,000 nT. It can generate a DC~60 μT magnetic field in any direction along the three axes, with an accuracy of ±0.01% at the center of the coil. The magnetic field strength of the device was adjusted in steps of 10,000 nT before observing whether the magnetometer output magnetic field value was correct. As indicated in Table 2, the test results suggest that the proposed probe exceeds the dynamic range of current commercial instruments of the same type.

Figure 23. Ultra-high-uniformity magnetic field generation system.

7.6. Triaxial Flux Gate Probe Testing

The core indicators of the triaxial flux gate probe, including zero-field offset compensation and noise, were tested and compared with those of a leading instrument, the Mag-03SS (Bartington Instruments Ltd., Witney, UK) [27]. The test results are presented in Table 3.

Table 3. A comparison of the test results of the triaxial flux gate probe with instruments of the same type.

Indicator	Proposed Triaxial Flux Gate Probe	Mag-03SS
Zero-field offset	$\leq\pm5$ nT	±30–±50 nT
Temperature drift compensation coefficient	$\leq\pm0.09$ nT/°C	$\leq\pm0.1$–±0.6 nT/°C
Polarity	Output voltage positive when pointing north	Output voltage positive when pointing north
Noise	$\leq$8 pT Hz$^{-1/2}$ rms at 1 Hz	6–20 pT Hz$^{-1/2}$ rms at 1 Hz
Frequency response and bandwidth	$\leq\pm3\%$ kHz^{-1}; $\geq$3 kHz	$\leq\pm5\%$ kHz^{-1}; $\geq$3 kHz
Scaling	100 mV/μT	100 mV/μT
Scaling error	$\leq\pm0.5\%$	$\leq\pm0.5\%$
Linearity error	<0.0015%	<0.0015%
Measurement range	±100 μT	±100 μT
Operating temperature	−40–85 °C	−10–50 °C
Orientation error	<0.5°	<0.5°
Installation error	<0.1°	<0.1°
Geomagnetic H, D, and Z components	High-precision continuous measurement	High-precision continuous measurement
Weight	80 g	185 g

7.7. Zero-Field Compensation of the Triaxial Flux Gate Probe

To eliminate the zero-field offset of the flux gate probe, the probe was placed in a zero-magnetic-field environment. The magnetic field strength output by the sensor in this environment represented the local zero-field compensation of the sensor. Specifically, the magnetic field reproduction system that is shown in Figure 24 was adopted for testing. The flux gate probe under test was placed at the center of the torque free coil within the magnetic shielding cylinder. A current of 0.08 mA was applied to the coil, generating a magnetic field of 8.88 nT within the shielding cylinder, and the flux gate was powered on.

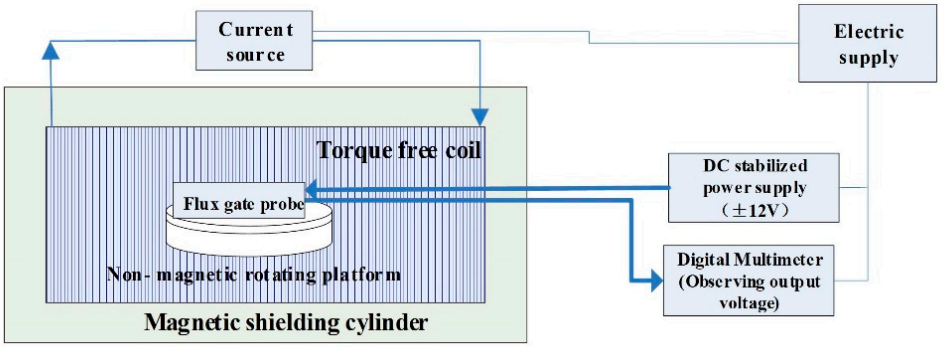

Figure 24. A schematic diagram of zero-field compensation testing for the triaxial flux gate probe.

The forward output voltage U_+ and the reverse output voltage U_- of the probe in the shielding cylinder were recorded. The zero-field compensation of the probe was calculated using Equation (3):

$$B_{offset} = \frac{U_+ + U_-}{2k_B} \tag{3}$$

where U_+ and U_- represent the forward and reverse output voltages of the target flux gate probe at zero magnetic field, respectively (μV), and k_B is the commutation coefficient of the target flux gate probe (μV/nT).

The above steps were repeated for the other two axes. The results are presented in Table 4, which indicates that the zero-field compensation is $\leq \pm 5$ nT.

Table 4. The zero-magnetic-field compensation test results of the triaxial flux gate probe.

Axis	Forward Output (μV)	Reverse Output (μV)	Commutation (μV/nT)	Zero-Field Compensation (nT)
X	−1169	1932	100	3.815
Y	480	390	100	4.350
Z	−2260	3250	100	4.950

7.8. Noise of the Triaxial Flux Gate Probe

The flux gate probe was placed in a zero-magnetic-field environment, and the background noise output by the probes was considered to be the sensor noise. The testing procedure is illustrated in Figure 25.

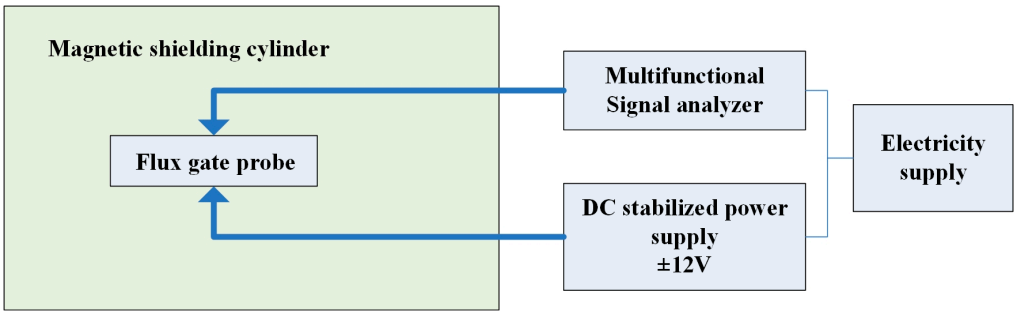

Figure 25. A schematic diagram of triaxial flux gate probe noise testing.

A spectrum analyzer was employed to measure the power spectral density, and the value at the 1 Hz frequency point was recorded as the output voltage noise level of the flux gate probe at that frequency point. Different frequency points were selected. The output voltage noise at each frequency point was then divided by the sensitivity at that frequency point. The equivalent input magnetic field noise at each frequency point was obtained using Equation (4):

$$B_N = \frac{U}{K_B} \tag{4}$$

where B_N is the noise of the calibrated flux gate probe, U is the average output voltage value from ten readings of the calibrated flux gate probe, and K_B is the commutation coefficient of the calibrated flux gate probe. The test results, which indicate that the noise of the triaxial flux gate probe is $\leq$8 pT $Hz^{-1/2}$, are indicated in Table 5.

Table 5. The noise test results of the triaxial flux gate probe.

Axis	Commutation Coefficient (μV/nT)	Output Voltage (μV $Hz^{-1/2}$)	Noise (pT $Hz^{-1/2}$)
X	100	597.298	5.97
Y	100	767.073	7.67
Z	100	590.630	5.91

7.9. Probe Automatic Switching Test

On 29 January 2024, the automatic switching scheme was tested using a drone platform carrying the probe in Zigong, Sichuan, China. During the test, the probe was mounted on the wing of the drone, and flights were conducted in multiple directions with various attitude changes. Throughout this process, magnetic field data from the three probes and the processed output data after the three-to-one selection were effectively collected.

The movement trajectory of the test platform is shown in Figure 26, the attitude of the test platform is shown in Figure 27, and the measured magnetic field curves during the test are presented in Figure 28. The first three graphs show the magnetic field intensity measured by each of the three probes. When one probe enters the dead zone, the system automatically switches to a probe that is not in the dead zone and selects its data. Therefore, the fourth graph represents the result of the automatic selection output, which appears as a relatively stable line. The initial oscillation and ascent process occurs when the drone is on a ferromagnetic cart on the ground, causing strong interference. From the test results' analysis, the automatic switching scheme for the three probes demonstrated the ability to operate without loss of lock in any heading globally, thus ensuring the continuity of magnetic field data collection.

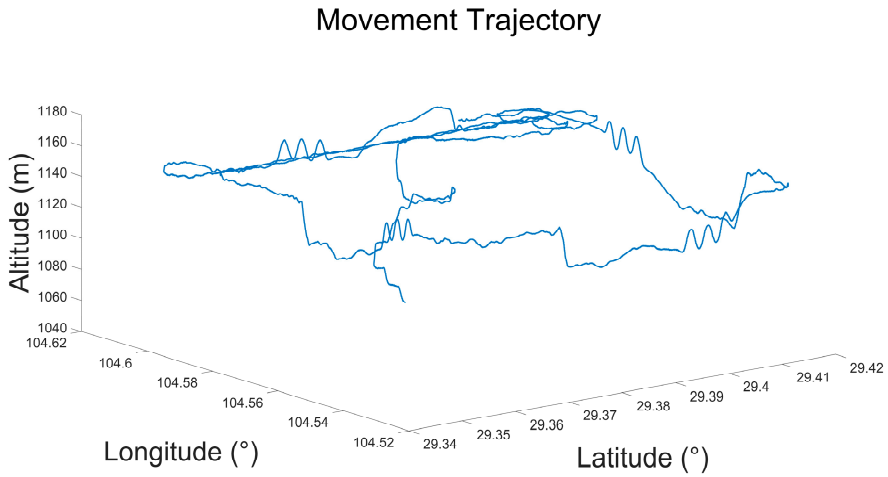

Figure 26. Platform movement trajectory.

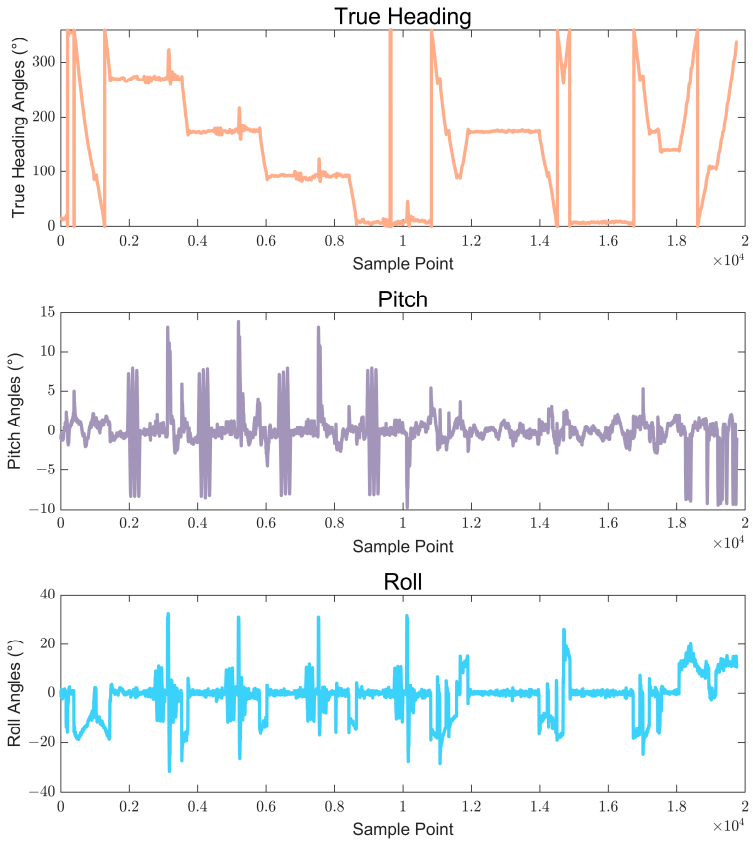

Figure 27. Platform movement attitude.

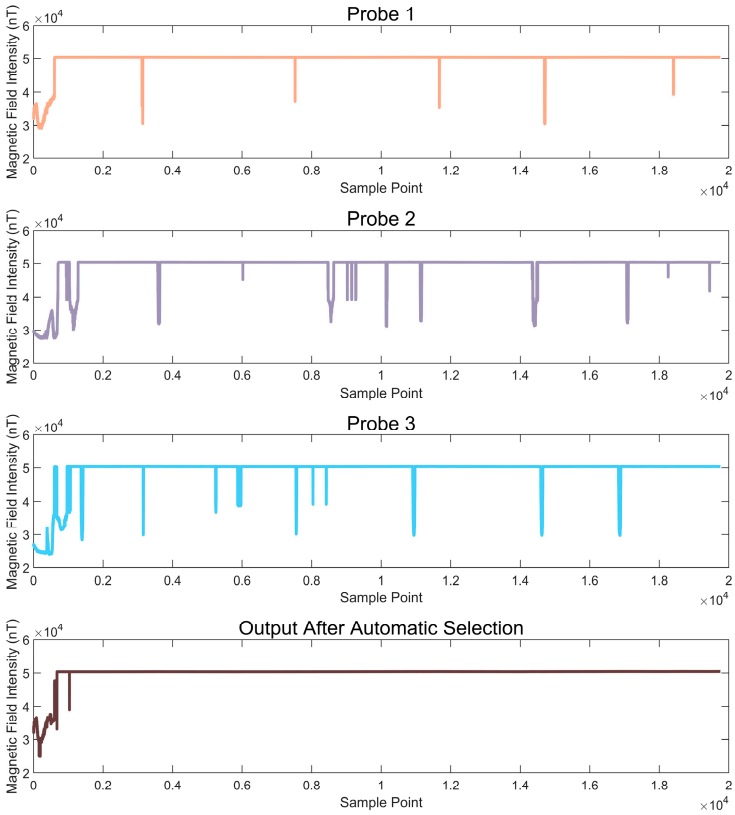

Figure 28. Test curves for the automatic probe switching experiment.

8. Conclusions

This paper provided a detailed introduction to the hardware design of a high-precision magnetic measurement system based on HOV technology. The system utilized an optically pumped cesium magnetometer to achieve high-precision magnetic field detection, while a three-component fluxgate probe was used to compensate for magnetic field interference caused by changes in the attitude of the HOV platform. The hardware design of the system was described in detail, and the key technical indicators of the system were rigorously tested and analyzed. The technical indicators of the proposed system were compared with those of advanced commercially available instruments of the same type, including the CS-3 and G-824A. The results demonstrate significant improvements in several key areas. Our magnetometer showed lower sensitivity (0.29 pT @ 1 sample/s), greater gradient tolerance ($\geq$54,000 nT/m), a wider dynamic range (12,165.10–137,992.85 nT), and a lighter weight (1.49 kg) while maintaining comparable overall performance in other aspects. Enhancing these indicators can substantially improve measurement accuracy and reliability, allowing magnetometers to operate stably in complex magnetic field environments and adapt to a wide range of magnetic field measurement needs, ranging from the extremely weak to extremely strong. Finally, drone-mounted tests verified that the automatic switching scheme for the three probes can prevent the magnetometer from entering a loss of lock state, ensuring the continuity of magnetic field data collection.

Author Contributions: Data curation, Q.Z. (Qimao Zhang); Formal analysis, K.Z.; Funding acquisition, Q.Z. (Qimao Zhang) and Q.Z. (Qisheng Zhang); Investigation, K.Z.; Methodology, Q.Z. (Qimao Zhang) and Q.Z. (Qisheng Zhang); Project administration, Q.Z. (Qimao Zhang) and Q.Z. (Qisheng Zhang); Resources, Q.Z. (Qimao Zhang); Supervision, Q.Z. (Qisheng Zhang); Validation, Q.Z. (Qimao Zhang); Writing—original draft, K.Z.; Writing—review and editing, K.Z. All authors have read and agreed to the published version of the manuscript.

Funding: This study is supported by the Key Research Program of the Chinese Academy of Sciences (Grant No. KGFZD-145-22-06-02), the National Key R&D Program of China (Grant No.

2022YFF0706202 and No. 2021YFC2801404), and the National Natural Science Foundation of China (Grant No. 42074155).

Data Availability Statement: Data is contained within the article.

Conflicts of Interest: The authors declare no conflicts of interest.

References

1. Wang, Z.; Liu, S.; Guo, Y.; Wu, Y.; Wang, Y.; Zhao, J. Joint use of scalar and vector magnetometers for underwater magnetic target localization. *IEEE Geosci. Remote Sens. Lett.* **2023**, *20*, 7505305. [CrossRef]
2. Li, X.; Luo, X.; Deng, M.; Qiu, N.; Sun, Z.; Chen, K. Low-noise, low-power-consumption seafloor vector magnetometer. *J. Oceanol. Limnol.* **2023**, *41*, 804–815. [CrossRef]
3. Wang, G.; Pan, Z. Fluxgate Magnetometer Offset Vector Determination Using Current Sheets in the Solar Wind. *Astrophys. J.* **2022**, *926*, 12. [CrossRef]
4. Sato, T.; Okino, K.; Kumagai, H. Magnetic structure of an oceanic core complex at the southernmost Central Indian Ridge: Analysis of shipboard and deep-sea three-component magnetometer data. *Geochem. Geophys. Geosyst.* **2009**, *10*, Q06003. [CrossRef]
5. Subba Rao, P.B.V.; Singh, B.P.; Gawali, P.B. A geoelectrical section across the Andaman arc sea region, northeast Indian Ocean by using ocean bottom magnetometers. *J. Geol. Soc. India* **2000**, *55*, 47–64.
6. Li, G.; Geng, X.; Liang, S.; Chen, Y.; Huang, G.; Li, G.; Zhang, X.; Yang, G. Attitude-independent route tracking for subsea power cables using a scalar magnetometer under high sea conditions. *Remote Sens.* **2024**, *16*, 226. [CrossRef]
7. Hori, S.; Oida, T.; Kobayashi, T. A simulation study on receivers of ultra-low field MRI with an optically pumped magnetometer. *Trans. Jpn. Soc. Med. Biol. Eng.* **2021**, *59*, 840–842.
8. Zhang, W.; Huang, W.; Luo, Y.; Li, F. Simultaneous detection of deep-sea earthquake and magnetic field using three-axis fiber optic accelerometer-magnetometer. In Proceedings of the 2019 IEEE International Instrumentation and Measurement Technology Conference, Auckland, New Zealand, 20–23 May 2019. [CrossRef]
9. Hood, L.L.; Oliveira, J.S.; Galluzzi, V.; Rothery, D.A. Investigating sources of Mercury's crustal magnetic field: Further mapping of MESSENGER magnetometer data. *J. Geophys. Res. Planets* **2018**, *123*, 2647–2666. [CrossRef]
10. Johnson, C.L.; Mittelholz, A.; Langlais, B.; Lognonne, P.; Pike, W.T.; Joy, S.P.; Russel, C.T.; Yu, Y.; Fillingim, M.; Ansan, V.; et al. First results from the InSight Fluxgate magnetometer: Constraints on Mars' crustal magnetic field at the InSight landing site. In Proceedings of the Lunar and Planetary Science Conference, The Woodlands, TX, USA, 18–22 March 2019.
11. Egbert, G.D.; Booker, J.R. Imaging crustal structure in southwestern Washington with small magnetometer arrays. *J. Geophys. Res. B Solid Earth* **1993**, *98*, 15967–15985. [CrossRef]
12. Richmond, N.C.; Hood, L.L. A preliminary global map of the vector lunar crustal magnetic field based on Lunar Prospector magnetometer data. *J. Geophys. Res.* **2008**, *113*, E02010. [CrossRef]
13. Gavazzi, B.; Alkhatib-Alkontar, R.; Munschy, M.; Colin, F.; Duvette, C. On the use of Fluxgate 3-axis magnetometers in archaeology: Application with a multi-sensor device on the site of Qasr 'Allam in the Western Desert of Egypt. *Archaeol. Prospect.* **2017**, *24*, 59–73. [CrossRef]
14. Cui, W. An overview of submersible research and development in China. *J. Mar. Sci. Appl.* **2018**, *17*, 459–470. [CrossRef]
15. Ge, J.; Luo, W.; Dong, H.; Liu, H.; Wang, H.; Wang, W.; Yuan, Z.; Zhu, J.; Zhang, H. Towed Overhauser marine magnetometer for weak magnetic anomaly detection in severe ocean conditions. *Rev. Sci. Instrum.* **2020**, *91*, 035112. [CrossRef] [PubMed]
16. Yu, C.; Xiang, X.; Lapierre, L.; Zhang, Q. Robust Magnetic Tracking of Subsea Cable by AUV in the Presence of Sensor Noise and Ocean Currents. *IEEE J. Ocean. Eng.* **2018**, *43*, 311–322. [CrossRef]
17. Jin, K.; Geng, X.; Liang, Z.; Tang, W.; Xiao, J.; Hu, H.; Huang, G.; Li, G.; Yang, G.; Liang, S. Design of Portable Self-Oscillating VCSEL-Pumped Cesium Atomic Magnetometer. *Electronics* **2022**, *11*, 3666. [CrossRef]
18. Ji, Z.H.; Zhang, H.S.; Su, D.Q.; Zhao, Y.T.; Xiao, L.T.; Jia, S.T. Pump–probe and four-wave mixing spectra arising from recoil-induced resonance in an operating cesium magneto-optical trap. *J. Phys. Soc. Jpn.* **2018**, *87*, 024301. [CrossRef]
19. Lu, Y.-T.; Liu, L.-S.; Shi, Y.-Q.; Zhao, T.; Zhu, W.-H.; Zhang, T.-F.; Liu, W.-M.; Zhang, X.-J. A High-Sensitivity Cesium Atomic Magnetometer Based on A Cesium Spectral Lamp. *Appl. Sci.* **2023**, *13*, 8225. [CrossRef]
20. Luong, V.S.; Le, M.; Quang, V.P. Fluxgate-based displacement sensor design. *J. Supercond. Novel Magn.* **2023**, *36*, 1767–1775. [CrossRef]
21. Cerdeira, M.A.; Kurlyandskaya, G.V.; Fernandez, A.; Tejedor, M.; Garcia-Miquel, H. Giant Magnetoimpedance Effect in Surface Modified CoFeMoSiB Amorphous Ribbons. *Chin. Phys. Lett.* **2003**, *20*, 2246–2249. [CrossRef]
22. Lotfollahi, Z.; Amirabadizadeh, A.; Safronov, A.P.; Kurlyandskaya, G.V. Magnetic properties and giant magnetoimpedance effect for CoFeMoSiB surface modified amorphous ribbons covered by water based ferrofluid. In Proceedings of the 7th Moscow International Symposium on Magnetism (MISM), Moscow, Russia, 1–5 July 2017.
23. Lotfollahi, Z.; Amirabadizadeh, A.; Safronov, A.P.; Beketov, I.V.; Kurlyandskaya, G.V. Magnetoimpedance effect in CoFeMoSiB as-quenched and surface modified amorphous ribbons in the presence of igon oxide nanoparticles of water-based ferrofluid. *J. Sens.* **2017**, *2017*, 4365682. [CrossRef]
24. Xilinx. Zynq-7000 SoC Technical Reference Manual. Available online: https://www.amd.com/en/products/adaptive-socs-and-fpgas/soc/zynq-7000.html (accessed on 1 January 2024).

25. Scintrex. Magnetic Methods. Available online: https://scintrexltd.com/wp-content/uploads/2017/03/CS-3-Brochure-762711_3.pdf (accessed on 5 June 2024).
26. Geometrics. G-824A Magnetometer. Available online: https://www.geometrics.com/product/g-824a/ (accessed on 5 June 2024).
27. Bartington Instruments. Mag-03® Three-Axis Magnetic Field Sensors. Available online: https://gmw.com/wp-content/uploads/2023/04/Mag-03-DS0013.pdf (accessed on 5 June 2024).